Binary nickel iron phosphide composites with oxidized surface groups as efficient electrocatalysts for the oxygen evolution reaction †

Article · November 2019

CITATIONS
0

READS
24

10 authors, including:

Han Zhu
Jiangnan University
4 PUBLICATIONS **0** CITATIONS
SEE PROFILE

Hao Jican
Jiangnan University
7 PUBLICATIONS **36** CITATIONS
SEE PROFILE

Shuanglong lu
Jiangnan University
37 PUBLICATIONS **391** CITATIONS
SEE PROFILE

Fang Duan
Jiangnan University
55 PUBLICATIONS **937** CITATIONS
SEE PROFILE

Sustainable Energy & Fuels

PAPER

View Article Online
View Journal

Cite this: DOI: 10.1039/c9se00445a

Binary nickel iron phosphide composites with oxidized surface groups as efficient electrocatalysts for the oxygen evolution reaction†

Chen Liu,[a] Han Zhu,*[a] Zhili Zhang,[a] Jican Hao,[a] Yudong Wu,[b] Jibiao Guan,[b] Shuanglong Lu,[a] Fang Duan,[a] Ming Zhang[b] and Mingliang Du*[a]

Electrocatalytic water splitting has become an effective approach to produce hydrogen as a clean energy source. Developing electrocatalysts for the oxygen evolution reaction (OER) with high efficiency and low cost is crucial for hydrogen energy systems due to the sluggish kinetics of OER. Herein, we have synthesized binary NiFeOH, NiFeO and NiFeP two-dimensional (2D) nanosheets on carbon cloth (CC) *via* a facile hydrothermal method combined with phosphorization and oxidation treatments. The porous binary NiFeP nanosheets exhibit an OER overpotential of 281 mV to achieve 20 mA cm^{-2} and a small Tafel slope of 74 mV dec^{-1}, which are lower than those of NiFeO (336 mV and 81 mV dec^{-1}). After the continuous OER operation for 50 h, the NiFeP-32/CC exhibits a small degradation of the current density (88% remains). The results indicate that large amounts of NiO and NiOOH phases formed on the NiFeP nanosheets during the OER process. The electrocatalytic activity for oxidized NiFeP with NiO and NiOOH phases is higher than that of pure NiFeO and NiFeOH, indicating that the synergistic effects among the NiFeP, NiO and NiOOH phases could improve the OER activity.

Received 5th July 2019
Accepted 4th October 2019

DOI: 10.1039/c9se00445a

rsc.li/sustainable-energy

Introduction

Hydrogen (H_2) has the potential to become a promising candidate to replace the fossil fuels due to its highly efficient, clean and sustainable features.[1–4] Among all the methods to generate H_2, electrochemical water splitting in alkaline solutions has aroused extensive attention in the field of sustainable hydrogen energy.[5–9] Generally, the hydrogen evolution reaction (HER) at the cathode and the oxygen evolution reaction (OER) at the anode are the basic components of the electrocatalytic water splitting. Although noble metals and their oxides, such as Pt-, Ir- and Ru-based metal catalysts, display superior performance for both half-reactions, the scarcity and high cost hinder their commercial deployment.[10–15] Therefore, it is important to develop earth-abundant and cost-effective electrocatalysts with excellent catalytic activity to achieve large-scale practical applications.

Due to the complicated multielectron transfer process and sluggish kinetics of OER, the overall efficiency of water splitting is impeded. Transition metal oxides (TMO) have been prepared as the efficient OER catalysts,[15–18] such as NiO,[19] Co_3O_4 (ref. 20) and CoO,[21] due to their low-cost, great stability and high electrocatalytic performance. However, there is still substantial room for improvement in both preparation techniques and the electrochemical performance of the catalysts. To further enhance the activity of electrocatalysts, exploring the non-oxide transition metals has been considered as a promising approach for OER.[22–26] Recently, transition metal phosphides (TMP)[27–31] have been proved to be promising candidates for active OER catalyst with superior electrochemical activity, owing to their intrinsic electronic structures, moderate price and good conductivity. The P species are not purely bystanders, and these species can offer positive connection to the reaction intermediates.[32] However, the limited active sites and lack of stability during OER catalysis still limit the wide application of TMPs. In this regard, the morphology regulation[33,34] and metal doping[35–39] of TMP materials are considered as two effective strategies for enhancing the electrocatalytic activity. The introduction of transition metals can modify electronic states and rearrange valence electrons, thus promoting the catalytic performance. In addition, the TMP catalysts are usually called as pre-catalysts due to the unclear active sites during the OER process.[38,40–42] Therefore, our goal is to provide a catalyst model for comparing the electrocatalytic activity of TMO and TMP and then design a potential electrocatalyst with minimal overpotential and preferable stability.

Herein, we have successfully synthesized the binary NiFeOH, NiFeO and NiFeP two-dimensional (2D) nanosheets on carbon cloth (CC) *via* a facile hydrothermal method combined with

[a]Key Laboratory of Synthetic and Biological Colloids, Ministry of Education, School of Chemical and Material Engineering, Jiangnan University, Wuxi 214122, P. R. China. E-mail: zhysw@jiangnan.edu.cn; du@jiangnan.edu.cn

[b]Key Laboratory of Advanced Textile Materials and Manufacturing Technology of the Ministry of Education, College of Materials and Textiles, Zhejiang Sci-Tech University, Hangzhou 310018, P. R. China

† Electronic supplementary information (ESI) available. See DOI: 10.1039/c9se00445a

phosphorization and oxidation treatment to identify the real active site for OER. The porous binary NiFeP nanosheets exhibit an OER overpotential of 281 mV to achieve 20 mA cm^{-2} and a small Tafel slope of 74 mV dec^{-1}, which are lower than those of NiFeO (336 mV and 81 mV dec^{-1}). After the continuous OER operation for 50 h, the NiFeP-32/CC exhibits a small degradation of the current density (88% remain). XPS and TEM results indicate that large amounts of NiO and NiOOH phases formed on the NiFeP nanosheets during the OER process, which serve as new active sites. The electrocatalytic activity of oxidized NiFeP with NiO and NiOOH is higher than that of the pure NiFeO and NiFeOH, indicating the synergistic effects among the NiFeP, NiO and NiOOH phases.

Experimental

Synthesis of NiFeOH precursor supported on CC

A carbon cloth (WOS1009, Taiwan) (3 × 3 cm) was pre-treated in HNO_3 and H_2SO_4 mixed solution with a volume ratio of 1 : 3 for 6 h. The carbon cloth (CC) after treatment was washed with water and ethanol, and then dried at 60 °C. 0.75 mmol $Ni(NO_3)_2 \cdot 6H_2O$ and $Fe(NO_3)_3 \cdot 9H_2O$ were dissolved in 20 mL of ethanol to form the NiFe precursor solution. The CC and 3 mmol urea dissolved in methanol (20 mL) were also added into the NiFe precursor solution and the mixture was kept under magnetic stirring for 15 min. The resulting solution was transferred into a 50 mL Teflon-lined stainless steel autoclave. The autoclave was heated at 180 °C for 16–18 h. After cooling naturally to room temperature, the NiFe(OH) precursor anchored on CC was obtained and washed with water for several times and then dried under air at 60 °C for 12 h. The initial ratios of the Ni and Fe source in the preparation of the NiFe precursor are 4 : 1, 3 : 2, 1 : 1 and 1 : 4, respectively.

Synthesis of NiFeP and NiFeO nanosheets supported on CC

The NiFeOH-xy precursor and 300 mg of NaH_2PO_2 were placed at the downstream and the upstream sides of the tube furnace. The samples were heated at 100 °C for 1 h at a heating rate of 5 °C min^{-1} in an Ar flow atmosphere, followed by heat treatment at 300 °C for 1 h at a heating rate of 1 °C min^{-1}. The NiFeP nanosheet grown on CC (denoted as NiFeP-xy/CC) was finally obtained. The NiP/CC and FeP/CC were also prepared according to the same method. In addition, the NiFeO-xy/CC was obtained through the oxidation process at 300 °C for 1 h. The NiFeP-32/CC was treated at 500 °C and 700 °C for 1 h in an Ar flow atmosphere to obtain NiFeP-32-500/CC and NiFeP-32-700/CC, respectively. The NiFeO-32/CC was treated at 500 °C for 1 h in air atmosphere to obtain NiFeO-32-500/CC.

Characterization

X-ray diffraction (XRD) patterns of the as-prepared samples were recorded with an X-ray diffractometer (Bruker AXS D8 DISCOVER) by Cu K_α radiation ($\lambda = 1.5406$ Å) at room temperature. X-ray photoelectron spectroscopy (XPS) measurements were performed with an X-ray photoelectron spectrometer (Kratos Axis Ultra DLD) using monochromatic Al K_α radiation as the excitation source (1486.6 eV), which was operated at 15 kV and 10 mA. The morphologies of the samples were captured by using a JSM-2100 transmission electron microscope (TEM) system (JEOL, Japan) with an acceleration voltage of 200 kV and a scanning electron microscope (SEM) system (JEOL, Japan) with an acceleration voltage of 3 kV. The Brunauer–Emmett–Teller (BET) surface areas of the products were determined using a nitrogen adsorption analyzer (ASAP2460, Micromeritics Instrument, USA), and the pore-size distribution was estimated by the Barrett–Joyner–Halenda method.

Electrochemical characterization

An electrochemical workstation (CHI660E, Shanghai Chenhua) was used to obtain the electrochemical measurements in 1.0 M KOH solution. All the electrochemical performance tests were performed with a standard three-electrode system, using the as-fabricated catalyst as the working electrode, a graphite rod as the counter electrode, and a saturated calomel electrode (SCE) as the reference electrode. In 1.0 M KOH solution, $E(\mathrm{RHE}) = E(\mathrm{SCE}) + 0.059\mathrm{pH} + 0.244$.

The preparation of the working electrode with a commercial catalyst is as follows: 14.13 mg of RuO_2 was dispersed in 882 μL of isopropanol solution (661.5 μL isopropanol and 220.4 μL water) under ultrasonication for 30 min. Subsequently, 118 μL of Nafion solution was added into the above solution with the assistance of ultrasonication for 30 min to form a homogeneous catalyst ink. The catalyst electrodes were obtained by doping approximately 5 μL solution on a glassy carbon (GC) with 0.07065 cm^2 of surface area. For the OER tests, the as-fabricated catalyst sheet surface area was controlled to be 0.4 cm^2 and the linear sweep voltammetry (LSV) was conducted with a scan rate of 5 mV s^{-1} in an alkaline medium. Before the LSV tests, all the catalysts were stabilized by the cyclic voltammogram (CV). All the LSV curves were treated by *iR* correction, which was calculated according to the equation $E_{\mathrm{corrected}} = E_{\mathrm{uncorrected}} - iR_{\mathrm{s}}$, where R_{s} is the measured solution resistance from electrochemical impedance spectroscopy (EIS) tests. The values of R_{s} are 3.42 Ω (NiFeP-32/CC), 3.40 Ω (NiO/CC), 8.9 Ω (RuO_2/CC), 3.7 Ω (FeO/CC), 3.62 Ω (NiFeO-64/CC), 3.44 Ω (FeP/CC), 3.53 Ω (NiP/CC), 3.25 Ω (NiFeP-41/CC), 3.48 Ω (NiFeP-14/CC), 2.84 Ω (NiFeP-32-500/CC), 3.02 Ω (NiFeP-32-700/CC) and 4.02 Ω (NiFeO-32-500/CC). The EIS tests were executed at the open circuit voltage of each catalyst. The electrochemically active surface area (ECSA) was calculated based on the measured double-layer capacitance in the non-faradaic regime of cyclic voltammetry.[43] CV were conducted from 1.02 to 1.12 V *vs.* RHE and 0.77 to 0.97 V *vs.* RHE by changing scan rates (50, 100, 200, 400, 600 and 800 mV s^{-1}) for NiFeP-32/CC and NiFeO-32/CC. The double-layer capacitances (C_{dl}) were also measured *via* these CVs.

Results and discussion

Fig. S1a and b† indicate the morphology of pure carbon fiber with smooth surfaces and average size ranging from 7–12 μm. After the hydrothermal reaction of Ni and Fe precursor, the two-dimensional (2D) NiFe(OH) nanosheets were formed

throughout the surfaces of CC (Fig. 1a). TEM image in Fig. 1d suggest that the NiFeOH connect with each other and the nanosheets form 3D networks with high density of nanosheets. After the oxidation process at 300 °C for 1 h, the former NiFeOH were converted into NiFe oxides (NiFeO) and the nanosheets became relatively thinner (Fig. 1b). The 3D network structure still remained the same (Fig. 1e). As shown in Fig. 1c, NiFeP after phosphorization also exhibits the 2D nanosheet morphology. In addition, as shown in Fig. 1f, the NiFeP nanosheets became porous and there were few nanoparticles located on the surfaces of nanosheets. For comparison, NiOH/CC, NiO/CC, NiP/CC, FeOH/CC, FeO/CC and FeP/CC were also prepared. As shown in Fig. S2a–c,† the NiOH, NiO and NiP display the 2D nanosheet morphology and the size of the nanosheets are larger than those of the NiFeOH, NiFeO and NiFeP. NiP has a porous surface structure, indicating that the phosphorization process could improve the surface defects and active sites, which are essential for the OER. For the Fe-based catalysts, as shown in Fig. S2b–d,† the FeOH, FeO and FeP nanocrystals exhibit the nanoparticle morphology without any nanosheets. Therefore, the main matrix of the as-prepared NiFeOH, NiFeO and NiFeP nanosheets consists of NiOH, NiO and NiP, respectively. Fe can be used as the doping element through the hydrothermal and phosphorization reactions.[34]

The HRTEM image of NiFeOH (Fig. 1g) clearly indicates the lattice fringes with a spacing of 0.23 nm and 0.21 nm, corresponding to the (200) and (103) planes of $Ni(OH)_2$ (JCPDS no. 38-0715). The NiFeO nanosheets in Fig. 1h display the lattice fringes with a spacing of 0.21 and 0.24 nm, ascribing to the (200) and (111) planes of the NiO phase (JCPDS no. 47-1049). As shown in Fig. 1i, the NiFeP nanosheets exhibit the lattice fringes with spacings of 0.22 nm, 0.20 nm and 0.19 nm, respectively, which correspond to the (111) and (201) planes of Ni_2P (JCPDS no. 74-1385) and (210) plane of Fe_2P phase (JCPDS no. 27-1171). The results indicate that the major part of NiFeP is the Ni_2P nanosheets and the small nanoparticles supported on the nanosheets are Fe_2P. In addition, the Brunauer–Emmett–Teller (BET) analysis was used to deeply investigate the porous structure. As shown in Fig. S7,† the surface area of NiFeO-32/CC and NiFeP-32/CC are 1.37 and 8.36 $m^2\ g^{-1}$, respectively, indicating the porous structures of NiFeP nanosheets.

In order to investigate the chemical composition, the STEM-EDS mapping image of NiFeP/CC were obtained, and are shown in Fig. 2a. The distribution of Ni and P elements is in accordance with the nanosheets and the Fe element seems to be isolated in the Ni_2P nanosheets. XRD was used to investigate the crystal structures of the as-prepared electrocatalysts. As shown in Fig. 2b, for all the samples, the broad bands located at about 43° and 52° correspond to the CC. The XRD diffraction peaks of NiO/CC are observed at 36.8°, 42.9° and 62.3°, which can be indexed to the (100), (200) and (220) planes of the NiO phase (JCPDS no. 47-1049), respectively. For the FeO/CC sample, the characteristic peaks located at 32.8°, 35.5° and 49.3° are consistent with the standard pattern of the Fe_2O_3 phase (JCPDS no. 33-0664). It is interesting to note that NiFeO/CC only exhibits the main diffraction peaks of NiO phases located at 36.8°, 42.9° and 62.3° and there is no Fe_2O_3 phase observed. The results indicate that the Fe element is doped into the NiO nanosheets and there were no NiO and Fe_2O_3 phase co-exist.[37,44]

As shown in Fig. 2c, the NiP/CC and FeP/CC did not show any crystal peaks, suggesting the low crystallinity of Ni_2P and Fe_2P. For the NiFeP/CC, as shown in Fig. 2b, the NiFeP/CC has clear diffraction peaks at 40.8°, 44.6° and 47.3°, which are indexed to the (111), (201) and (210) crystal planes of Ni_2P (JCPDS no. 89-

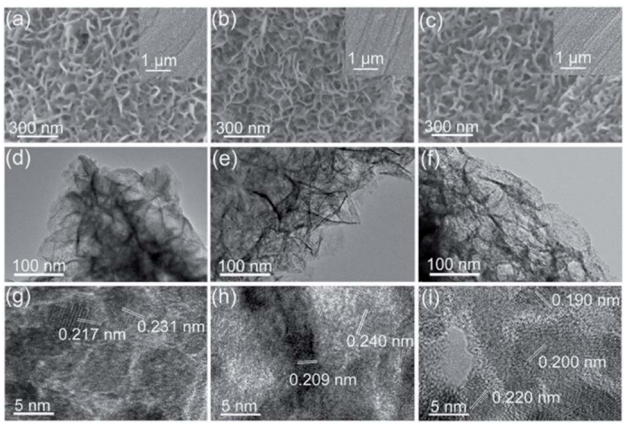

Fig. 1 FESEM, TEM and HRTEM images of (a, d and g) NiFeOH-32/CC, (b, e and h) NiFeO-32/CC, (c, f and i) NiFeP-32/CC.

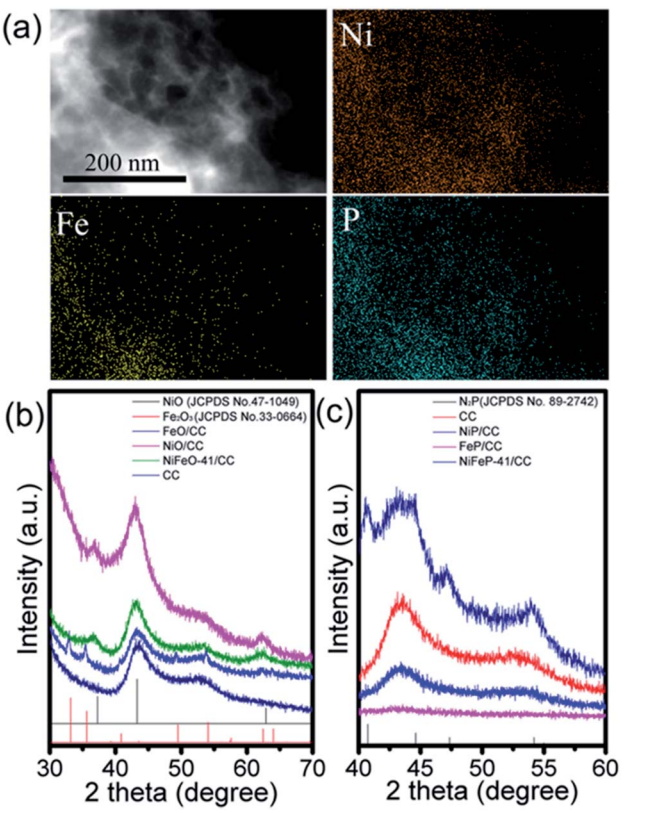

Fig. 2 (a) HAADF-STEM image and the corresponding STEM-EDS mapping images of the NiFeP/CC. (b) XRD patterns of CC, NiP/CC, FeP/CC and NiFeP/CC. (c) XRD patterns of CC, NiO/CC, FeO/CC and NiFeO/CC.

2742). There are no Fe_2P diffraction peaks observed due to the low crystallinity of Fe_2P. In addition, according to the STEM elemental mapping results and XRD results, the 2D nanosheets are composed of Ni_2P with certain amount of Fe_2P on the surfaces.

XPS was employed to investigate the chemical states and bonding states of the as-prepared catalysts. Fig. S4† indicates the XPS survey of NiFeP-32/CC, and Ni, Fe, P, C and O elements could be observed. Fig. 3a indicates the Ni 2p core-level XPS spectra of NiFeP-32/CC. The Ni 2p XPS spectra display two spin–orbit doublets located at 853.2 (Ni $2p_{3/2}$), 870.4 (Ni $2p_{1/2}$) and 856.4 (Ni $2p_{3/2}$), 874.3 eV (Ni $2p_{1/2}$), respectively, indicating that the atoms of Ni are in the divalent and trivalent states.[27] The two shake-up satellite peaks emerged at 879.5 eV and 861.7 eV. The Fe 2p core-level XPS spectra of NiFeP-32/CC are shown in Fig. 3b. The Fe 2p spectra present two spin–orbit doublet peaks located at the binding energies of 711.4, 714.8 eV and 724.3, 727.7 eV, which belong to the Fe $2p_{3/2}$ and Fe $2p_{1/2}$ of Fe^{2+} and Fe^{3+}.[35]

For the P 2p XPS spectra, the binding energy features two low intensity peaks located at 129.4 eV and 130.3 eV, suggesting the two chemical states of metal–phosphides (Ni–P and Fe–P). The peaks at 133.8 eV and 134.8 eV belong to the surface metal phosphate species in PO_4^{3-} arising from the superficial oxidation of the nickel and iron phosphide.[27,35] The result is similar to those in the previous literatures. In the O 1s XPS spectra (Fig. 3d), the two peaks located at 532.8 eV and 531.5 eV could be ascribed to the adsorbed H_2O and metal oxides or oxyhydroxides.[44]

The electrocatalytic OER performance of the as-prepared catalysts has been investigated by a three-electrode system in 1 M KOH. The as-fabricated catalyst was used as the working electrode, a graphite rod was used as the counter electrode, and a saturated calomel electrode (SCE) was used as the reference electrode. As shown in Fig. 4a, to reach the current density of 20 mA cm^{-2}, the individual FeP/CC and NiP/CC required the overpotentials of 388 and 392 mV. The NiFeP/CC only required a very low overpotential of 281 mV to obtain the current density of 20 mA cm^{-2}, which is lower than that of the commercial RuO_2/CC catalysts (345 mV). The results indicate that the 2D NiFeP nanosheets exhibit superior OER performance. Interestingly, the Ni^{2+}-to-Ni^{3+} oxidation peak appeared around 1.40 V *vs.* RHE in the LSV curves of the NiFeP/CC catalysts. According to the previous literature, the highest intensity oxidation peak in NiFeP nanosheets indicate the formation of numerous Ni^{3+} species and the corresponding NiOOH species might be regarded as the active sites, which is beneficial for boosting the OER performance.[42,45,46] Fig. 4b exhibits the polarization curves of the Ni, Fe and NiFe binary oxides supported on CC. The NiO/CC and FeO/CC need 434 mV and 513 mV, respectively, to reach the current density of 20 mA cm^{-2}. Similarly, the NiFeO/CC only requires an overpotential of 336 mV to obtain the current density of 20 mA cm^{-2}. The NiFeP/CC shows a lower overpotential of 281 mV than the NiFeO/CC (336 mV), indicating that the binary metal phosphides have a higher OER performance than the binary metal oxides.

We also prepared NiFeP/CC with different mass ratios of Ni and Fe. The NiFeP/CC samples were denoted as NiFeP-41/CC, NiFeP-32/CC, NiFeP-11/CC and NiFeP-14/CC. The SEM images of NiFeP-41/CC, NiFeP-11/CC and NiFeP-14/CC are shown in Fig. S3† and they all exhibit 2D nanosheet morphology. The corresponding OER performance is shown in Fig. 4c. As shown in Fig. 4c, the NiFeP-41/CC, NiFeP-11/CC and NiFeP-14/CC need overpotentials of 289, 328 and 337 mV to reach the current density of 20 mA cm^{-2}, respectively. In addition, the NiFeP-32/CC exhibits the best OER activity with an overpotential of 281 mV. It is indicated that the high mass ratio of Ni would lead to a relatively lower overpotential for OER and the best mass ratio of Ni and Fe is found to be 3 : 2. The calculated overpotentials for the all prepared catalysts are shown in Fig. 4d–f.

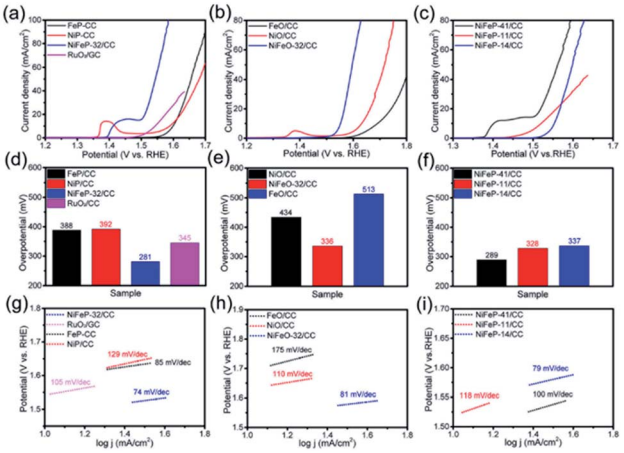

Fig. 4 (a) Polarization curves obtained for the FeP/CC, NiP/CC, NiFeP-32/CC and the commercial RuO_2/CC. (b) Polarization curves obtained for the FeO/CC, NiO/CC, and NiFeO-32/CC. (c) Polarization curves obtained for the NiFeP-41/CC, NiFeP-11/CC and NiFeP-14/CC. (d–f) The corresponding overpotential of the as-prepared catalysts obtained at a current density of 20 mA cm^{-2}. (g–i) The corresponding Tafel plots of the as-prepared catalysts.

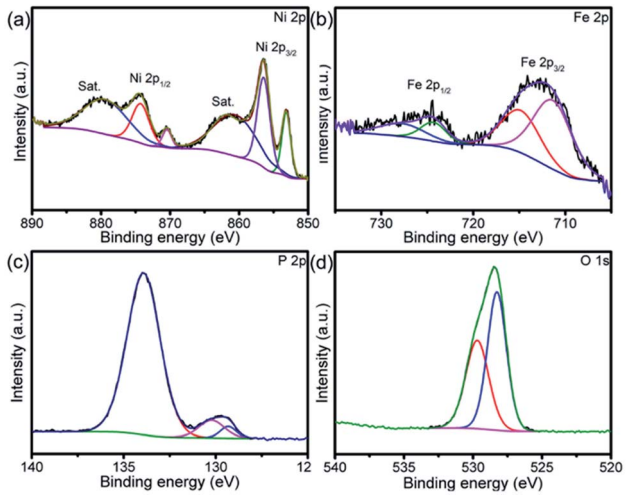

Fig. 3 (a) Ni 2p, (b) Fe 2p, (c) P 2p and (d) O 1s XPS spectra of NiFeP-32/CC.

In addition, the NiFeP-32-700/CC requires the overpotential of 298 mV (Fig. S8†) to reach 20 mA cm^{-2}, indicating that high temperature treatment can influence the OER performance.

Tafel slope is an important characterization for OER catalysts to evaluate the catalysis kinetics. As shown in Fig. 4g–i, the NiFeP-32/CC, NiP/CC, FeP/CC and RuO_2/CC obtained the Tafel slopes of 74, 85, 129 and 105 mV dec^{-1}, respectively. The NiFeO/CC, NiO/CC and FeO/CC obtained the Tafel slopes of 85, 110, and 175 mV dec^{-1}, respectively. As shown in Fig. 4i, the NiFeP-41/CC, NiFeP-11/CC and NiFeP-14/CC obtained the Tafel slopes of 100, 118, and 79 mV dec^{-1}, respectively. The NiFeP-32/CC exhibits the smallest Tafel slope of 74 mV dec^{-1}, which is smaller than that of the commercial RuO_2/CC (105 mV dec^{-1}), suggesting the fast kinetics process. The electrochemical impedance spectroscopy (EIS) has also been investigated. As shown in Fig. S5,† the Nyquist plots indicate that NiFeP-32/CC possesses a much smaller charge-transfer impedance of 3 Ω at open circuit potential, suggesting the fast electron transport.

Many literatures have previously reported that the metal phosphides are pre-catalysts that will be transformed into metal oxo/hydroxo species after the continuous OER performance at relatively high current density.[45–50] To investigate the change of catalyst during the OER process, the SEM and TEM images of NiFeP-32/CC obtained after the stability test for 50 h are shown in Fig. 5a and b. Compared with the initial NiFeP-32/CC (Fig. 1c), the NiFeP-32/CC after the stability test still exhibits the 2D morphology with porous surfaces. The surface changing were attributed to the partial oxidation of NiFeP nanosheets during the OER process. The HRTEM images of NiFeP-32/CC after the stability test are shown in Fig. 5c and d. These images display the lattice fringes with interplanar distances of about 0.25 and 0.21 nm, which could be attributed to the (200) and (111) planes of the Ni_2P phase, respectively.[51] The lattice spacings of 0.24 nm and 0.23 nm could be assigned to the (011) plane of NiOOH[52] and (111) plane of NiO[53] phase, respectively, suggesting the partial oxidation and hydroxide of NiFeP. The results indicate that after the stability test for 50 h, the main nanosheets still exist and NiO or NiOOH species formed during the oxygen evolution reaction as reported.[50]

The XPS spectra of NiFeP-32/CC after the stability test for 50 h are shown in Fig. 6. From the Ni 2p XPS spectra (Fig. 6a), compared with the initial NiFeP-32/CC spectra shown in Fig. 3a, the binding energies for Ni $2p_{1/2}$ and Ni $2p_{3/2}$ shift to 855.6, 873.2 and 856.9, 874.8 eV, which are ascribed to Ni^{2+} and Ni^{3+}.[54] As shown in Fig. 6b, the Fe 2p spectra has two spin–orbit doublet peaks located at the binding energies of 712.7, 717.1 eV and 725.4, 727.7 eV, which belong to the Fe $2p_{3/2}$ and Fe $2p_{1/2}$ of Fe^{2+} and Fe^{3+}.[35] For the P 2p XPS spectra, the P signal reduce sharply on the surface states, suggesting the oxidation of NiFeP during the OER process. We found that the phosphorus anion in NiFeP is depleted in the active form of the electrocatalyst and that the surface of NiFeP is converted into an amorphous NiFe oxide including NiO, FeO and NiOOH species. This XPS results indicate that the surface of the NiFeP nanosheets are partially converted to NiFe oxides with an oxide or oxo-hydroxide overlayer. The formed NiFeP–NiFeO interfaces could help in better carrier transportation from the core NiFeP to the surface NiFeO oxides. Meanwhile, the higher-valent P species that are formed during the OER catalysis may act as a P ligand on the catalyst. The O 1s XPS spectrum has two peaks at 531.9 eV and 531.4 eV. According to some reports, the O element can be ascribed to M–OH.[54]

The XPS results indicate that after the continuous OER operation, there are a certain amount of NiOOH and NiO phase formed due to oxidation. Therefore, in order to investigate the difference in the electrocatalytic activity of the oxidized NiFeP and NiFeO, we obtained the OER LSV curves of oxidized NiFeP and NiFeO. The current–time curves of NiFeP-32/CC for OER performed at 1.575 V *vs.* RHE in 1.0 M KOH display outstanding electrochemical stability (Fig. 7a) and the current density display small degradation over more than 50 h (with about 12% loss), suggesting the strong stability. As shown in Fig. 7b, the LSV curves of NiFeP before and after the stability test for 50 h remain almost unchanged with the current density degrading

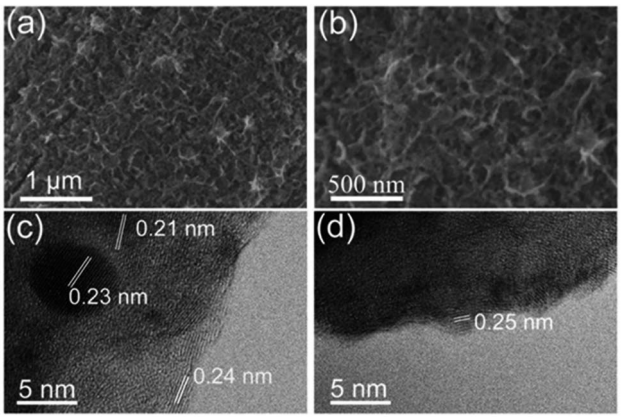

Fig. 5 (a and b) SEM images of NiFeP-32/CC obtained after stability test for 50 h. (c and d) HRTEM images of the NiFeP-32/CC obtained after stability test for 15 h.

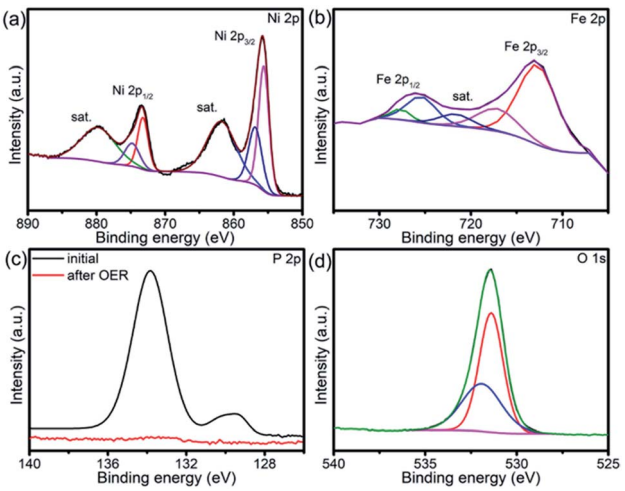

Fig. 6 (a) Ni 2p, (b) Fe 2p, (c) P 2p, and (d) O 1s XPS spectra of NiFeP-32/CC after stability test for 50 h.

slightly. The overpotential of NiFeP after the stability test for 50 h is 289 mV at 20 mA cm^{-2}, which is only 8 mV higher than the initial NiFeP catalyst.

The electrochemical surface area (ECSA) of the NiFe-based electrocatalysts were roughly estimated from C_{dl} by measuring CV curves at different scan rates in a non-faradaic region (Fig. S6†). As shown in Fig. 7c, the double-layer capacitance (C_{dl}) of the initial NiFeP-32/CC, NiFeP-32/CC after stability and NiFeO-32/CC are 2.03 mF cm^{-2}, 1.08 mF cm^{-2} and 0.8 mF cm^{-2}. Therefore, the ECSA corresponding to the catalysts are 9.875, 18.75 and 7.36 cm^2, respectively. The ECSA of NiFeP-32/CC after stability (18.75 cm^2) is higher than that of the initial NiFeP-32/CC (9.875 cm^2) and NiFeO-32/CC (7.36 cm^2), manifesting the larger surface area.

This result demonstrates that the formation of numerous NiO species and NiOOH species on NiFeP nanosheets could be the new active site, which is beneficial for boosting the OER performance. The LSV curves for NiFeP-32/CC after stability test and NiFeO-32/CC are shown in Fig. 7d. The NiFeP-32/CC after stability requires 389 mV to reach the current density of 20 mA cm^{-2}, which is very lower than that of NiFeO-32/CC (336 mV at 20 mA cm^{-2}). The binary metal phosphides with good efficiency and corrosion stability for the OER are related to a heterostructure where metal oxo/hydroxo species are formed on the surface of the catalyst due to the surface oxidation of metal phosphides. Compared to NiO/CC and FeO/CC, the higher performance of NiFeP-32/CC with the new NiOOH phase indicate that the Fe doping indeed improve the electrocatalytic activity. The results indicate that even though the large amount of P is oxidized, the electrocatalytic activity of oxidized NiFeP with NiO and NiOOH phases are still higher than that of pure NiFeO, suggesting that the NiOOH phases are the new active sites. The electro-catalytic activity for oxidized NiFeP with NiO and NiOOH is higher than the pure NiFeO and NiFeOH, indicating the synergistic effects among the NiFeP, NiO and NiOOH phases.

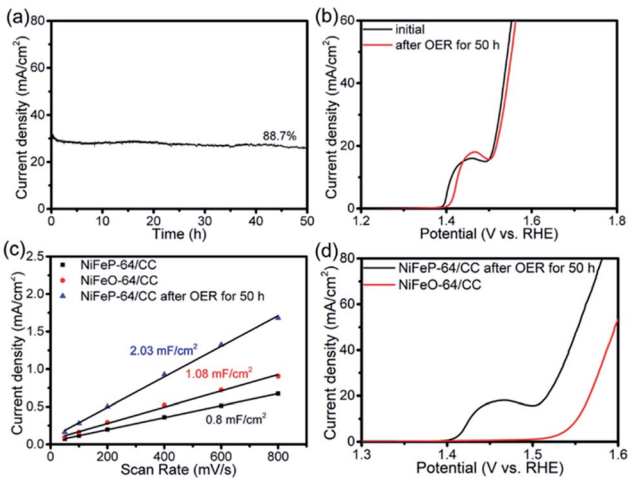

Fig. 7 (a) The current–time curves of NiFeP-32/CC in 1.0 M KOH. (b) OER polarization curves of NiFeP-32/CC before and after continuous stability test for 50 h. (c) Plots of the capacitive currents as a function of scan rate of the as-prepared catalysts (d) OER polarization curves of NiFeP-32/CC after the stability test for 50 h and NiFeO-32/CC.

Conclusions

In summary, we have successfully synthesized the binary NiFeOH, NiFeO and NiFeP 2D nanosheets on carbon cloth *via* a facile hydrothermal method combined with phosphorization and oxidation treatment to identify the real active site for OER. Compared with NiFeOH and NiFeO, the porous NiFeP nanosheets exhibit large surface area and favorable electrical conductivity and show higher electrocatalytic performance for OER in 1.0 M KOH electrolyte, together with superior electrochemical stability for more than 50 h. The porous binary NiFeP nanosheets exhibit an OER overpotential of 281 mV to achieve 20 mA cm^{-2} and a small Tafel slope of 74 mV dec^{-1}, which are lower than those of NiFeO (336 mV and 81 mV dec^{-1}). After the continuous OER operation for 50 h, the NiFeP-32/CC exhibits a small degradation of the current density (88% remain). XPS and TEM results indicate that large amounts of NiO and NiOOH phases formed on the NiFeP nanosheets during the OER process. The results indicate that even though a large amount of P is oxidized, the electrocatalytic activity for the oxidized NiFeP with NiO and NiOOH phases are still higher than the pure NiFeO, suggesting that the NiOOH phases are the new active sites. The electrocatalytic activity for oxidized NiFeP with NiO and NiOOH is higher than that of the pure NiFeO and NiFeOH, indicating the synergistic effects among the NiFeP, NiO and NiOOH phases.

Conflicts of interest

There are no conflicts to declare.

Acknowledgements

This study was supported by the National Natural Science Foundation of China (NSFC) (Grant no. 51573166, 51803077), Natural Science Foundation of Jiangsu Province (Grant no. BK20180627), China Postdoctoral Science Foundation (2018M630517, 2019T120389), the MOE & SAFEA, 111 Project (B13025), the national first-class discipline program of Light Industry Technology and Engineering (LITE2018-19), and the Fundamental Research Funds for the Central Universities.

Notes and references

1 R. Wu, J. Zhang, Y. Shi, D. Liu and B. Zhang, *J. Am. Chem. Soc.*, 2015, **137**, 6983–6986.
2 J. Ying, G. Jiang, Z. Paul Cano, L. Han, X.-Y. Yang and Z. Chen, *Nano Energy*, 2017, **40**, 88–94.
3 J. Wang, W. Cui, Q. Liu, Z. Xing, A. M. Asiri and X. Sun, *Adv. Mater.*, 2016, **28**, 215–230.
4 Q. Lu, Y. Yu, Q. Ma, B. Chen and H. Zhang, *Adv. Mater.*, 2016, **28**, 1917–1933.
5 Z. Zou, X. Wang, J. Huang, Z. Wu and F. Gao, *J. Mater. Chem. A*, 2019, **7**, 2233–2241.

6 K. Xu, H. Ding, M. Zhang, M. Chen, Z. Hao, L. Zhang, C. Wu and Y. Xie, *Adv. Mater.*, 2017, **29**, 1606980.
7 X. Long, H. Lin, D. Zhou, Y. An and S. Yang, *ACS Energy Lett.*, 2018, **3**, 290–296.
8 Y. Hou, M. Qiu, T. Zhang, X. Zhuang, C. S. Kim, C. Yuan and X. Feng, *Adv. Mater.*, 2017, **29**, 1701589.
9 H. Zhu, G. Gao, M. Du, J. Zhou, K. Wang, W. Wu, X. Chen, Y. Li, P. Ma, W. Dong, F. Duan, M. Chen, G. Wu, J. Wu, H. Yang and S. Guo, *Adv. Mater.*, 2018, **30**, e1707301.
10 H. Jiang, J. Gu, X. Zheng, M. Liu, X. Qiu, L. Wang, W. Li, Z. Chen, X. Ji and J. Li, *Energy Environ. Sci.*, 2019, **12**, 322–333.
11 W. Chen, Y. Zhang, G. Chen, R. Huang and K. Ostrikov, *J. Mater. Chem. A*, 2019, **7**, 3090–3100.
12 I. S. Amiinu, X. Liu, Z. Pu, W. Li, Q. Li, J. Zhang, H. Tang, H. Zhang and S. Mu, *Adv. Funct. Mater.*, 2018, **28**, 1704638.
13 K. Qu, Y. Zheng, Y. Jiao, X. Zhang, S. Dai and S.-Z. Qiao, *Adv. Energy Mater.*, 2017, **7**, 1602068.
14 H. Zhu, J. Zhang, R. Yanzhang, M. Du, Q. Wang, G. Gao, J. Wu, G. Wu, M. Zhang, B. Liu, J. Yao and X. Zhang, *Adv. Mater.*, 2015, **27**, 4752–4759.
15 P. Zhou, J. He, Y. Zou, Y. Wang, C. Xie, R. Chen, S. Zang and S. Wang, *Sci. China: Chem.*, 2019, 1–6.
16 N. T. Suen, S. F. Hung, Q. Quan, N. Zhang, Y. J. Xu and H. M. Chen, *Chem. Soc. Rev.*, 2017, **46**, 337–365.
17 K. Fominykh, G. C. Tok, P. Zeller, H. Hajiyani, T. Miller, M. Döblinger, R. Pentcheva, T. Bein and D. Fattakhova-Rohlfing, *Adv. Funct. Mater.*, 2017, **27**, 1605121.
18 H. Zhu, L. Gu, D. Yu, Y. Sun, M. Wan, M. Zhang, L. Wang, L. Wang, W. Wu, J. Yao, M. Du and S. Guo, *Energy Environ. Sci.*, 2017, **10**, 321–330.
19 K. Fominykh, J. M. Feckl, J. Sicklinger, M. Döblinger, S. Böcklein, J. Ziegler, L. Peter, J. Rathousky, E.-W. Scheidt, T. Bein and D. Fattakhova-Rohlfing, *Adv. Funct. Mater.*, 2014, **24**, 3123–3129.
20 L. Mei, X. Huang, X. Wen, J. Ding, B. Liu, Y. Du and J. Xue, *Nano Energy*, 2017, **33**, 445–452.
21 X. Yuan, H. Ge, W. Xin, C. Dong and F. Huang, *ACS Energy Lett.*, 2017, **2**, 1208–1213.
22 Z. Jin, P. Li and D. Xiao, *Green Chem.*, 2016, **18**, 1459–1464.
23 F. Ling, W. Li, Y. Guan, Y. Feng and W. Yu, *Adv. Funct. Mater.*, 2017, **27**, 1701008.
24 L. Wei, X. Gao, D. Xiong, W. Fang, W. G. Song, J. Xu and L. Liu, *Adv. Energy Mater.*, 2017, **7**, 1602579.
25 T. Wang, G. Nam, Y. Jin, X. Wang, P. Ren, M. G. Kim, J. Liang, X. Wen, H. Jang, J. Han, Y. Huang, Q. Li and J. Cho, *Adv. Mater.*, 2018, **30**, e1800757.
26 X. Xu, F. Song and X. Hu, *Nat. Commun.*, 2016, **7**, 12324.
27 T. Liu, A. Li, C. Wang, W. Zhou, S. Liu and L. Guo, *Adv. Mater.*, 2018, **30**, e1803590.
28 Y. Li, J. Chen, P. Cai and Z. Wen, *J. Mater. Chem. A*, 2018, **6**, 4948–4954.
29 Y. Lin, Y. Li, Y. Zhang, H. Jiang, Z. Xiao, C. Wu, G. Zhang, J. Jiang and S. Li, *Adv. Energy Mater.*, 2018, 1703623.
30 T. Meng, Y. N. Hao, L. Zheng and M. Cao, *Nanoscale*, 2018, **10**, 14613–14626.
31 Y. Zou, Z. Liu, R. Liu, D. Liu, C. Dong, Y. Wang and S. Wang, *J. Power Sources*, 2019, **427**, 215–222.
32 A. Dutta and N. Pradhan, *J. Phys. Chem. Lett.*, 2017, **8**, 144–152.
33 M. Liu and J. Li, *ACS Appl. Mater. Interfaces*, 2016, **8**, 2158–2165.
34 W. T. Hong, M. Risch, K. A. Stoerzinger, A. J. L. Grimaud, S. Jin and S. H. Yang, *Energy Environ. Sci.*, 2015, **8**, 1404–1427.
35 Y. Li, H. Zhang, M. Jiang, Q. Zhang, P. He and X. Sun, *Adv. Funct. Mater.*, 2017, **27**, 1702513.
36 Y. Pei, Y. Yang, F. Zhang, P. Dong, R. Baines, Y. Ge, H. Chu, P. M. Ajayan, J. Shen and M. Ye, *ACS Appl. Mater. Interfaces*, 2017, **9**, 31887–31896.
37 C. Tang, R. Zhang, W. Lu, L. He, X. Jiang, A. M. Asiri and X. Sun, *Adv. Mater.*, 2016, **29**, 1602441.
38 B. Zhang, Y. H. Lui, H. Ni and S. Hu, *Nano Energy*, 2017, **38**, 553–560.
39 T. Liu, X. Ma, D. Liu, S. Hao, G. Du, Y. Ma, A. M. Asiri, X. Sun and L. Chen, *ACS Catal.*, 2016, **7**, 98–102.
40 J. Xu, X.-K. Wei, J. D. Costa, J. L. Lado, B. Owens-Baird, L. P. L. Gonçalves, S. P. S. Fernandes, M. Heggen, D. Y. Petrovykh, R. E. Dunin-Borkowski, K. Kovnir and Y. V. Kolen'ko, *ACS Catal.*, 2017, **7**, 5450–5455.
41 J. Y. Xu, J. P. S. Sousa, N. E. Mordvinova, J. D. Costa and Y. V. Kolen'Ko, *ACS Catal.*, 2018, **8**, 2595–2600.
42 L.-A. Stern, L. Feng, F. Song and X. Hu, *Energy Environ. Sci.*, 2015, **8**, 2347–2351.
43 X. Lu and C. Zhao, *Nat. Commun.*, 2015, **6**, 6616.
44 Q. Zhang, D. Yan, Z. Nie, X. Qiu, S. Wang, J. Yuan, D. Su, G. Wang and Z. Wu, *ACS Appl. Mater. Interfaces*, 2018, **1**, 571–579.
45 G. F. Chen, T. Y. Ma, Z. Q. Liu, N. Li, Y. Z. Su, K. Davey and S. Z. Qiao, *Adv. Funct. Mater.*, 2016, **26**, 3314–3323.
46 P. Wang, Z. Pu, Y. Li, L. Wu, Z. Tu, M. Jiang, Z. Kou, I. S. Amiinu and S. Mu, *ACS Appl. Mater. Interfaces*, 2017, **9**, 26001–26007.
47 J. Masa, S. Barwe, C. Andronescu, I. Sinev, A. Ruff, K. Jayaramulu, K. Elumeeva, B. Konkena, B. Roldan Cuenya and W. Schuhmann, *ACS Energy Lett.*, 2016, **1**, 1192–1198.
48 S. Yao, V. Forstner, P. W. Menezes, C. Panda, S. Mebs, E. M. Zolnhofer, M. E. Miehlich, T. Szilvasi, N. Ashok Kumar, M. Haumann, K. Meyer, H. Grutzmacher and M. Driess, *Chem. Sci.*, 2018, **9**, 8590–8597.
49 J. Luo, H. Wang, G. Su, Y. Tang, H. Liu, F. Tian and D. Li, *J. Mater. Chem. A*, 2017, **5**, 14865–14872.
50 P. He, X. Y. Yu and X. W. Lou, *Angew. Chem., Int. Ed.*, 2017, **56**, 3897–3900.
51 X. Wang, Y. V. Kolen'ko and L. Liu, *Chem. Commun.*, 2015, **51**, 6738–6741.
52 L. Yan, H. Jiang, Y. Xing, Y. Wang, D. Liu, X. Gu, P. Dai, L. Li and X. Zhao, *J. Mater. Chem. A*, 2018, **6**, 1682–1691.
53 X. Wei, Y. Zhang, H. He, D. Gao, J. Hu, H. Peng, L. Peng, S. Xiao and P. Xiao, *Chem. Commun.*, 2019, **55**, 6515–6518.
54 W. Gu, L. Hu, X. Zhu, C. Shang, J. Li and E. Wang, *Chem. Commun.*, 2018, **54**, 12698–12701.